International Journal of Power Electronics and Drive Systems (IJPEDS)
Vol. 12, No. 3, September 2021, pp. 1620~1631
ISSN: 2088-8694, DOI: 10.11591/ijpeds.v12.i3.pp1620-1631

Modeling and control of a hybrid DC/DC/AC converter to transfer power under different power management strategies

Amin Alizadeh Asl[1], Ramin Alizadeh Asl[2]
[1]Department of Electrical and Computer Engineering, Tabriz University, Iran
[2]Department of Electrical Engineering, Urmia University, Iran

Article Info

Article history:

Received Feb 21, 2021
Revised Jun 22, 2021
Accepted Jul 14, 2021

Keywords:

DC/DC/AC converter
Decentralized multivariable control method
FACTS
PV/FC/battery hybrid power systems
Three-input DC-DC converter

ABSTRACT

A hybrid DC/DC/AC converter connected to the grid without a three-phase transformer is controlled. The decentralized control method is applied to the hybrid DC-DC converter such that the maximum power of PV flows to the grid side. This controller must charge and discharge the battery at the proper time. It must also regulate DC-link voltage. An additional advantage of the proposed control is that the three-phase inverter does not need a separate controller such as PWM and SPWM. A simple technique is used for creating the desired phase shift in the three-phase inverter, which makes the active and reactive power of the inverter controllable. A new configuration is also proposed to transmit and manage the generation power of PV. In this scheme, the battery and fuel cell are employed as an auxiliary source to manage the generation power of PV. Finally, a real-time simulation is performed to verify the effectiveness of the proposed controller and system by considering the real characteristics of PV and FC.

Corresponding Author:

Amin Alizadeh Asl
Departement of Electrical and Computer Engineering
Tabriz University
East Azerbaijan Province, Tabriz, 29 Bahman Boulevard, Iran
Email: aminalizadeh594@gmail.com

1. INTRODUCTION

The use of PV as a conventional resource will be possible in the future. PV can be combined with other clean energy sources, e.g., fuel cells and batteries [1]. Power electronic converters, which have recently made significant progress, are characterized by their high efficiency, high reliability, and merging different renewable energies [2]. The majority of the studies are on multi-input DC-DC converters in the field of power electronics. Ahrabi *et al* [3], Furkan Akar *et al* [4], Banaei *et al* [5], Danyali *et al*. [6], Ghavidel *et al*. [7], Parham Mohseni *et al* [8], Neng Zhang *et al* [9] have introduced a new, highly-efficient multi-input DC-DC converter suitable for renewable energies. The application of power electronic converters is expanding in modern power systems [10]-[16] due to the integration of renewable energy. While controlling transmission power had problems in conventional power systems, transmission power is controllable in modern systems. Problems associated with real-time control of transmission power are major factors leading to blackout in traditional power systems, especially when the grid faces cascade outages [17]-[24]. Nowadays, the lack of a suitable controller makes the system approaches to collapse. However, the control of transmission power between two busbars is almost impossible in conventional power systems. By employing power electronic converters, the transmission power can be controlled, and immediate action becomes possible for the operator.

This paper focuses on the control issues of transmission power. The flexibility and high reliability in transferring power are the features of the proposed system. An advanced DC-DC converter, three-phase inverter, and the multivariable decentralized control technique are utilized for this purpose.

There is little research on controlling DC-DC converters connected to a three-phase inverter to transfer the maximum power of renewable sources. A suitable multivariable control technique should be adopted because power electronic converters are multivariable systems. The control method must extract the maximum power of PV and simultaneously control active and reactive power. Khaki-Sedigh, and Moaveni [25] has delineated different multivariable control techniques, and this paper has employed a decentralized control technique to control the proposed system. Figure 1 shows the proposed system.

The operation of modern power systems has faced new challenges upon the expanded integration of PVs. On the one hand, the maximum power of PV must be extracted at any moment to be economically justified. On the other hand, uncertainty in PV generation will cause problems, including balancing in power generation and consumption. Therefore, herein, a hybrid structure consisting of a battery and fuel cell is utilized to control the transferring power proportional to the demanded power while the maximum power of PV is extracted. A compromise can be made between uncertainty in the generation power of PV and the power required by the grid via the proposed hybrid structure; if the output power of PV is more than the demanded power, the proposed controller must charge the battery, and if power demanded by the network is more than the output power of PV, the control system must add a fuel cell and battery to the structure to transfer the set power to the network.

The proposed system and controller pursue several objectives simultaneously:

a. Extracting the maximum output power of PV at any moment
b. Managing transmission power with the help of the battery and FC (without disturbing the maximum power extraction of PV)
c. Regulating DC-link voltage

The important point in this structure is that the transmission power does not affect the extraction of the maximum power of PV.

First, the dynamic model of a hybrid DC-DC converter is achieved. Then, a suitable controller is designed. Subsequently, the phase-shift technique is applied to a three-phase inverter to transfer the set power. Finally, extensive simulation is prepared to validate the proper performance of the proposed system. Furthermore, fast fourier transform (FFT) analysis is conducted in each mode to present detailed results of the proposed system.

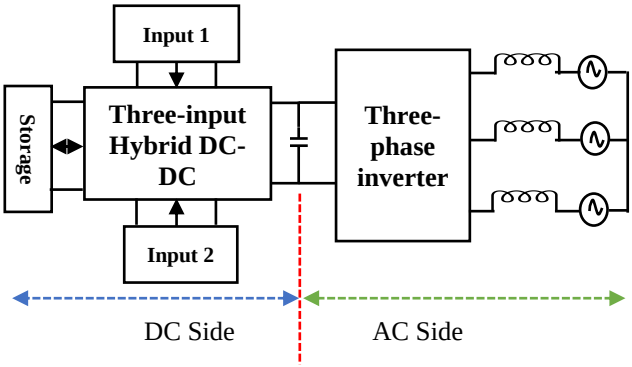

Figure 1. General scheme of the proposed system

2. SMALL-SIGNAL MODELING OF HYBRID DC/DC/AC CONVERTER

Figure 2 displays the hybrid DC-DC converter that is the inverter input. Since the output voltage and current of the DC-DC converter are DC, the inverter and grid or the AC side are modeled only with simple resistance $R_L=V_O/I_O$. However, the designed controller is applied to the true system to verify the effectiveness of the controller. According to Figure 2, it is clear that a discontinuous current is imposed on PV, which disturbs the maximum power point tracking. A conventional buck-boost is allocated at the entrance of V_2; consequently, $I_{PV}=I_{L2}\times d_2$. Thus, this problem can be solved by controlling I_{L2}; in this case, the maximum power of PV is followed. The proposed system has three modes.

In the first mode, PV and FC can produce the desired consumption power, so the battery must be bypassed. In this mode, it is assumed that the requested power by grid is more than the maximum power of PV. In the second mode, the total generation power of PV and FC cannot supply the output, so the battery is

discharged. In the third mode, it is assumed that the whole generation power of PV and FC is larger than the required consumption power in the output stage, so the surplus energy is saved in the battery. A separate controller must be designed in each mode because the state-space model of the system is different. All three modes cover the reality in the grid. Therefore, in first step, the controller must identify the mode of operation and then in the second step, act such that the intended control objectives be achieved.

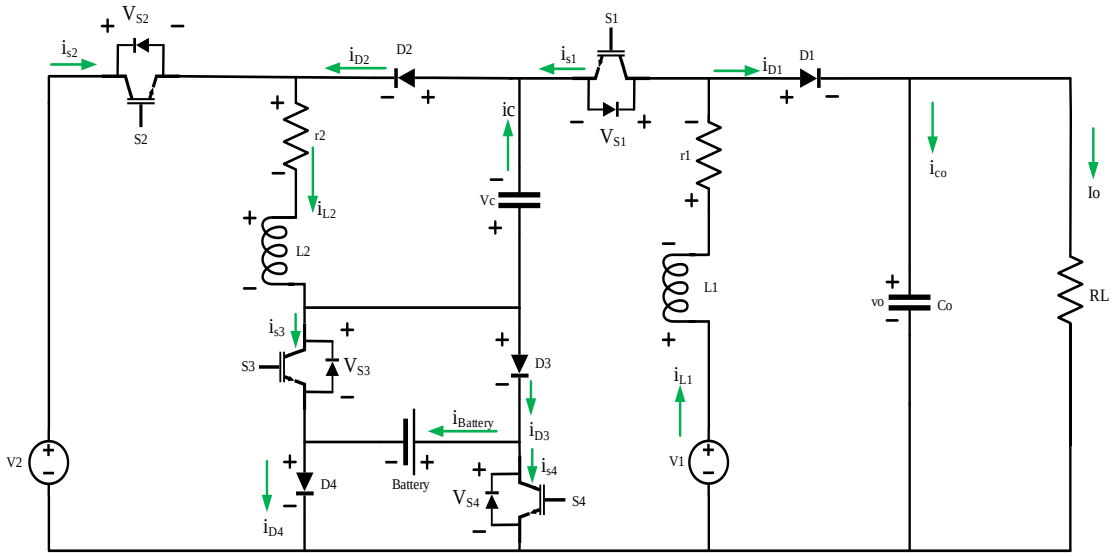

Figure 2. The Hybrid DC-DC Converter

2.1. First operation mode (Supplying the load without the contribution of the battery)

To bypass the battery in this mode, S3 and S4 must be turned off and turned on, respectively. Consequently, d_4 (duty cycle of S4) =1 and d_3 (duty cycle of S3) =0; thus, d_4 and d_3 as control signals are missed. Only d_1 (duty cycle of S1) and d_2 (duty cycle of S2) are utilized to extract the maximum power of PV and regulate the output voltage. Furthermore, (1) shows the state-space model of systems.

$$L_1\frac{di_{L1}}{dt} = -r_1 i_{L1} + (V_1 + V_C)d_1 + (V_1 - V_O)(1 - d_1), C\frac{dV_c}{dt} = (i_{L2} - i_{L1})(d_1 - d_2) - i_{L1}d_2 + i_{L2}(1\text{-}d_2)$$
$$L_2\frac{di_{L2}}{dt} = -r_2 i_{L2} + V_2 d_2 - V_C(1\text{-}d_2), C_o\frac{dV_o}{dt} = i_{L1}(1\text{-}d_1) - \frac{V_o}{R_L} \quad (1)$$

The (1) is driven from the principle of the voltage balance and current balance in the inductor and capacitor in the steady-state, respectively. Moreover, (1) reveals that reaching the transfer function matrix is impossible because the duty cycle of switches is directly related to state variables. The linearization technique at the operating point is a well-known technique for solving this problem. In this method, state variables, duty cycles, and inputs are divided into two component DC values ($\bar{X},\bar{V},\bar{D}$) and perturbation ($\tilde{x},\tilde{v},\tilde{d}$):

$$x = \bar{X} + \tilde{x}, v = \bar{V} + \tilde{v}, d = \bar{D} + \tilde{d} \quad (2)$$

If it is assumed that the perturbation is small and does not significantly vary during the switching period ($\tilde{x} << \bar{X}, \tilde{v} << \bar{V}, \tilde{d} << \bar{D}$), by substituting (2) into (1) and neglecting the second terms, small-signal models are represented in the matrix form as (3):

$$\dot{\tilde{x}} = A\tilde{x} + B\tilde{u}$$
$$\tilde{y} = C\tilde{x} + Du \quad (3)$$

where $\tilde{x}$, $\tilde{u}$, and $\tilde{y}$ are state variables' vector, control variables' vector, and the output system, respectively. Therefore, the matrix form of the small-signal model for the first mode is obtained as (4):

$$\begin{bmatrix} \frac{d\tilde{i}_{L1}}{dt} \\ \frac{d\tilde{i}_{L2}}{dt} \\ \frac{d\tilde{v}_c}{dt} \\ \frac{d\tilde{v}_o}{dt} \end{bmatrix} = \begin{bmatrix} \frac{-r_1}{L_1} & 0 & \frac{\bar{D}_1}{L_1} & \frac{-1+\bar{D}_1}{L_1} \\ 0 & \frac{-r_2}{L_2} & \frac{-1+\bar{D}_2}{L_2} & 0 \\ \frac{-\bar{D}_1}{C} & \frac{1-\bar{D}_2}{C} & 0 & 0 \\ \frac{1-\bar{D}_1}{C_O} & 0 & 0 & \frac{-1}{R_L C_O} \end{bmatrix} \begin{bmatrix} \tilde{I}_{L1} \\ \tilde{I}_{L2} \\ \tilde{V}_c \\ \tilde{V}_o \end{bmatrix} + \begin{bmatrix} \frac{\bar{V}_O+\bar{V}_C}{L_1} & 0 \\ 0 & \frac{\bar{V}_2+\bar{V}_C}{L_2} \\ \frac{-\bar{I}_{L1}}{C} & \frac{-\bar{I}_{L2}}{C} \\ \frac{-\bar{I}_{L1}}{C_O} & 0 \end{bmatrix} \begin{bmatrix} \tilde{d}_1 \\ \tilde{d}_2 \end{bmatrix}, y = \begin{bmatrix} 0100 \\ 0001 \end{bmatrix} \begin{bmatrix} \tilde{I}_{L1} \\ \tilde{I}_{L2} \\ \tilde{V}_c \\ \tilde{V}_o \end{bmatrix}; D = 0 \quad (4)$$

2.2. Second operation mode (Supplying the load with discharging the battery)

In this mode, the maximum power of PV and FC must be extracted, and the battery is connected to the system to regulate the output voltage. S4 must be kept turned on to discharge the battery. Moreover, the power flow to the battery is controlled by turning on and turning off S3. Furthermore, (5) expresses the state-space model of systems.

$$L_1 \frac{di_{L1}}{dt} = -r_1 i_{L1} + (V_1+V_C+V_B)d_3 + (V_1+V_C)(d_1-d_3) + (V_1-V_O)(1-d_1), C\frac{dV}{dt} = -i_{L1}d_2 + (i_{L2}-i_{L1})(d_1-d_2) + i_{L2}(1-d_1)$$
$$L_2 \frac{di_{L2}}{dt} = -r_2 i_{L2} + (V_2+V_B)d_3 + V_2(d_2-d_3) - V_C(1-d_2), C_o \frac{dV_o}{dt} = i_{L1}(1-d_1) - \frac{V_o}{R_L} \quad (5)$$

Similar to the first mode, the dynamic model is obtained as (6):

$$\begin{bmatrix} \frac{d\tilde{i}_{L1}}{dt} \\ \frac{d\tilde{i}_{L2}}{dt} \\ \frac{d\tilde{v}_c}{dt} \\ \frac{d\tilde{v}_o}{dt} \end{bmatrix} = \begin{bmatrix} \frac{-r_1}{L_1} & 0 & \frac{\bar{D}_1}{L_1} & \frac{-1+\bar{D}_1}{L_1} \\ 0 & \frac{-r_2}{L_2} & \frac{-1+\bar{D}_2}{L_2} & 0 \\ \frac{-\bar{D}_1}{C} & \frac{1-\bar{D}_2}{C} & 0 & 0 \\ \frac{1-\bar{D}_1}{C_O} & 0 & 0 & \frac{-1}{R_L C_O} \end{bmatrix} \begin{bmatrix} \tilde{i}_{L1} \\ \tilde{i}_{L2} \\ \tilde{v}_c \\ \tilde{v}_o \end{bmatrix} + \begin{bmatrix} \frac{\bar{V}_O+\bar{V}_C}{L_1} & 0 & \frac{\bar{V}_B}{L_1} \\ 0 & \frac{\bar{V}_2+\bar{V}_C}{L_2} & \frac{\bar{V}_B}{L_2} \\ \frac{-\bar{I}_{L1}}{C} & \frac{-\bar{I}_{L2}}{C} & 0 \\ \frac{-\bar{I}_{L1}}{C_O} & 0 & 0 \end{bmatrix} \begin{bmatrix} \tilde{d}_1 \\ \tilde{d}_2 \\ \tilde{d}_3 \end{bmatrix}, y = \begin{bmatrix} 1000 \\ 0100 \\ 0001 \end{bmatrix} \begin{bmatrix} \tilde{i}_{L1} \\ \tilde{i}_{L2} \\ \tilde{v}_c \\ \tilde{v}_o \end{bmatrix}; D = 0 \quad (6)$$

2.3. Third operation mode (Supplying the load with charging the battery)

The charge path is established by turning off the S4, and the current of the battery is controlled by turning on and off the S3. Moreover, (7) shows the state-space model of systems.

$$L_1 \frac{di_{L1}}{dt} = -r_1 i_{L1} + (V_1+V_C)d_3 + (V_1+V_C-V_B)(d_1-d_3) + (V_1-V_O)(1-d_1), C\frac{dV}{dt} = -i_{L1}d_2 + (i_{L2}-i_{L1})(d_1-d_2) + i_{L2}(1-d_1)$$
$$L_2 \frac{di_{L2}}{dt} = -r_2 i_{L2} + V_2 d_3 + (V_2-V_B)(d_2-d_3) - V_C(1-d_2), C_o \frac{dV_o}{dt} = i_{L1}(1-d_1) - \frac{V_o}{R_L} \quad (7)$$

Similar to the previous mode, the dynamic model is obtained as (8):

$$\begin{bmatrix} \frac{d\tilde{i}_{L1}}{dt} \\ \frac{d\tilde{i}_{L2}}{dt} \\ \frac{d\tilde{v}_c}{dt} \\ \frac{d\tilde{v}_o}{dt} \end{bmatrix} = \begin{bmatrix} \frac{-r_1}{L_1} & 0 & \frac{\bar{D}_1}{L_1} & \frac{-1+\bar{D}_1}{L_1} \\ 0 & \frac{-r_2}{L_2} & \frac{-1+\bar{D}_2}{L_2} & 0 \\ \frac{-\bar{D}_1}{C} & \frac{1-\bar{D}_2}{C} & 0 & 0 \\ \frac{1-\bar{D}_1}{C_O} & 0 & 0 & \frac{-1}{R_L C_O} \end{bmatrix} \begin{bmatrix} \tilde{I}_{L1} \\ \tilde{I}_{L2} \\ \tilde{V}_c \\ \tilde{V}_o \end{bmatrix} + \begin{bmatrix} \frac{\bar{V}_O+\bar{V}_C-\bar{V}_B}{L_1} & 0 & \frac{\bar{V}_B}{L_1} \\ 0 & \frac{\bar{V}_2+\bar{V}_C-\bar{V}_B}{L_2} & \frac{\bar{V}_B}{L_2} \\ \frac{-\bar{I}_{L1}}{C} & \frac{-\bar{I}_{L2}}{C} & 0 \\ \frac{-\bar{I}_{L1}}{C_O} & 0 & 0 \end{bmatrix} \begin{bmatrix} \tilde{d}_1 \\ \tilde{d}_2 \\ \tilde{d}_3 \end{bmatrix}, y = \begin{bmatrix} 1000 \\ 0100 \\ 0001 \end{bmatrix} \begin{bmatrix} \tilde{I}_{L1} \\ \tilde{I}_{L2} \\ \tilde{V}_c \\ \tilde{V}_o \end{bmatrix}; D = 0 \quad (8)$$

3. DESIGNING THE CLOSED-LOOP CONTROLLER AND EXAMINING ITS PERFORMANCE

In the first mode, the main control objectives were specified. I_{L2} is controlled to PV working at maximum power, and the output capacitor voltage is controlled to adjust the output voltage. As explained before, in the first mode, the duty cycle of S3 and S4 is missed as control signals, and only d_1 and d_2 are available as control signals due to bypassing the battery. Now, one must control state variables (I_{L2}, V_O) with d_1 or d_2. In multivariable control, control signals for each output (state variables) are selected by the relative gain array (RGA) matrix. The RGA is a widely-used classical method for determining the best input-output paring for the multivariable process control system. In its general form, the RGA matrix is defined as (9):

$$\Lambda(G(j\omega))=G(j\omega).*G(j\omega)^{-T} \quad (9)$$

The RGA matrix is calculated in the steady state as:

$$\Lambda(G(0))=G(0).*G^{-T}(0)=\begin{pmatrix}2.39 & -1.39\\ -1.39 & 2.39\end{pmatrix} \quad (10)$$

$$\Lambda(G(0))=G(0).*G^{-T}(0)=\begin{pmatrix}2.1365 & -3.2139 & 2.0774\\ 0 & 3.3333 & -2.3333\\ -1.1365 & 0.8806 & 1.2559\end{pmatrix} \quad (11)$$

$$\Lambda(G(0))=G(0).*G^{-T}(0)=\begin{pmatrix}2.2656 & -1.4350 & 0.1694\\ 0 & 1.8224 & -0.8224\\ -1.2656 & 0.6126 & 1.6530\end{pmatrix} \quad (12)$$

(10), (11), and (12) are the RGA matrix for the first, second, and third modes, respectively.

The RGA matrix shows the dependency of the control signal to the output. In (10)-(12), diagonal elements have significant values compared to other elements, so it can be concluded that, in (10), d_1 and d_2 have the most impact on I_{L2} and V_O, respectively. However, being positive has a priority to the value in the RGA matrix. Therefore, pairing the input-output set is defined as follow:

First mode: $I_{L2} \rightarrow d_1 \quad V_O \rightarrow d_2$
Second and Third modes: $I_{L1} \rightarrow d_1 \quad I_{L2} \rightarrow d_2 \quad V_O \rightarrow d_3$

Figures 3 and 4 illustrate the closed-loop configuration in the first, second, and third mode. The most important part of the multivariable system is system coupling. In these schemes, the CP matrix is placed to decouple the system, and PI controllers undertake reference tracking. There are several options for designing the CP matrix, but in general form, CP depends on systems and the control objective. The CP is chosen as follows for decoupling the system in the steady state:

$$CP=[G(0)]^{-1} \quad (13)$$

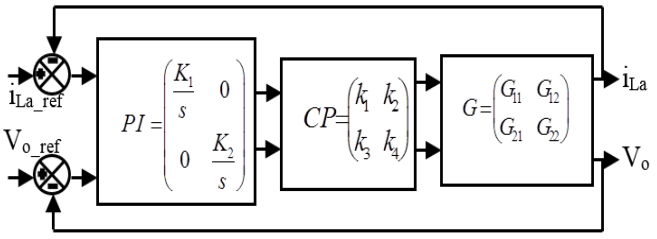

Figure 3. Scheme of closed-loop for first mode

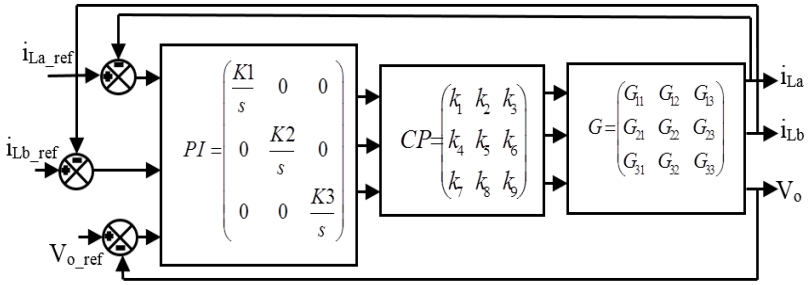

Figure 4. The closed-loop scheme for second and third modes

The closed-loop performance is simulated with the help of MATLAB/SIMULINK. Figure 5 shows the closed-loop performance in the first mode. In Figure 5, $U = [4\ 0]^T$ is applied to the system in the second moment. It is expected that Y_1 and Y_2 should have value due to the inherent coupling in multi-input systems. The CP matrix makes the system decouple in the steady state, and the PI controller causes reference tracking to occur. The accurate performance of the controller is evident because it managed to eliminate the intrinsic coupling in the system, and reference tracking happened simultaneously. All these features are achieved by a simple CP matrix and diagonal PI controller. Figures 6 and 7 demonstrate closed-loop performance in the second and third modes. Similar to the first mode, good performance has been achieved.

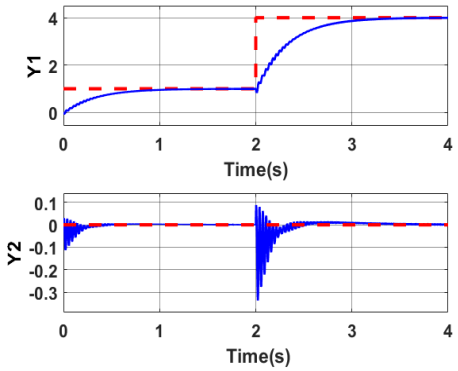

Figure 5. Closed-loop performance in the first mode

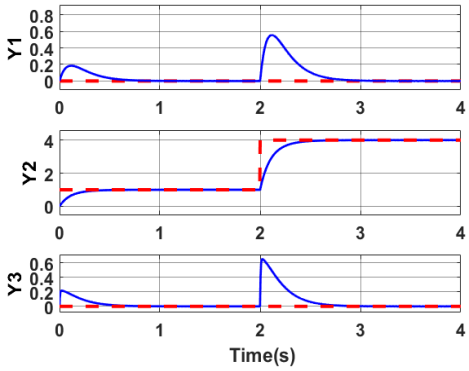

Figure 6. Closed-loop performance in the second mode

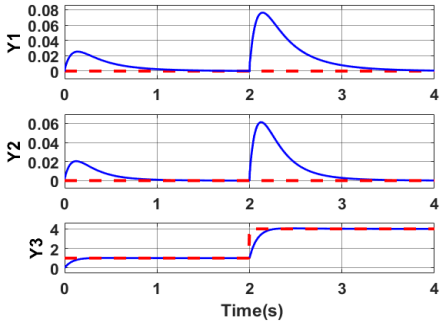

Figure 7. Closed-loop performance in the third mode

4. SIMULATION RESULTS

The closed-loop controller was designed in previous sections. In this section, the hybrid DC-DC converter is connected to a three-phase inverter to transfer the power of PV, FC, and battery to the grid. All modes are simulated by MATLAB/Simulink. Figures 8 and 9 display PV and FC characteristics, respectively. The ready block of PEMFC is a preset model for fuel cells in MATLAB/Simulink and has been employed in this paper.

The simulation consists of three modes. In the first mode, the sun irradiation of PV is S=500W/m^2, and under this condition, the maximum generation power of PV is about 10800 W, and it occurs at 300 V. Moreover, in this mode, the maximum power of FC equals 8325 W, and it happens at around 225 A. The battery is bypassed in this mode, and the total generation and transmission powers are assumed to be equal (10800+8325=19125 W).

In the second mode, the sun irradiation of PV is S=600 W/m^2, and the maximum power under this irradiation is 12950 W and takes place at 300 V. FC has 6000 W in the second mode, and under this power, FC can give nearly 133 A. The summation of powers from both sources equals 12950+6000=18950 W; therefore, in comparison to the first mode, the total generation power has decreased. Consequently, the battery must be added to the system to resolve the lack of power and converter losses.

In the third mode, the irradiation of PV is S=750 W/m^2, the maximum power of PV reaches about 16102 W, and the voltage of PV is close to 285 V. The power of FC is approximately 4284 W, and under this

power, FC can give 86 A. The total generation power from both sources equals 16102+4284=20386 W, which is larger than the demanded power for transferring. As a result, the battery must be charged to save surplus energy in the third mode.

The state variables of the hybrid DC-DC converter are controllable. Hence, I_{L1}, I_{L2}, and V_O must be controlled to extract the maximum power of resources besides regulating the DC-link voltage. The output voltage of the inverter depends on the DC-link voltage. Therefore, the inverter does not need to be controlled in a conventional way such as sinusoidal pulse width modulation. Furthermore, the output voltage of the inverter can be controlled by changing the DC-link voltage ($V_{an}=2V_{dc}/\pi$). The only parameter that must be controlled in the inverter is the phase difference. In all three modes, the inverter must be able to produce a +90º phase difference ($\delta = 90^o$); in this case, maximum active power is transferred from the DC side to the AC side.

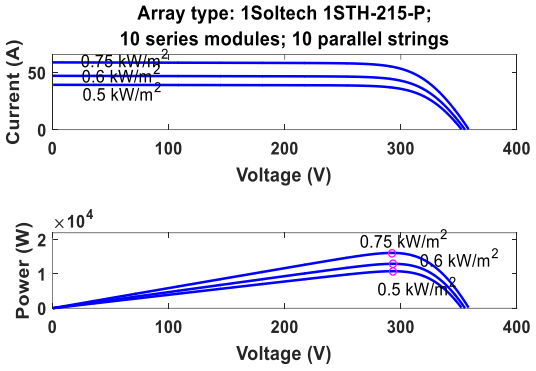

Figure 8. PV characteristics

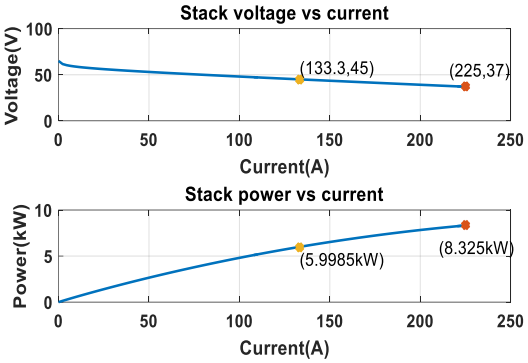

Figure 9. Fuel cell characteristics

A 6-s simulation with three power management strategies is provided to evaluate the proposed control system in each operation mode. Figure 10 and Figure 11 depict the duty cycles of S1, S2, S3, and S4, respectively, and show the control signals that vary to extract the maximum power of resources. Figure 12 represents the hybrid DC-DC converter outputs. The most important part of the control system is the duty cycles of the converter switches, which have been shown in Figure 10 and Figure 11 because the transient-state of the converter depends on the variation of duty cycles.

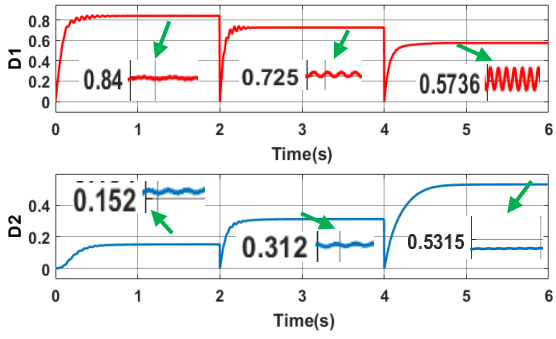

Figure 10. Duty cycles of S1 and S2

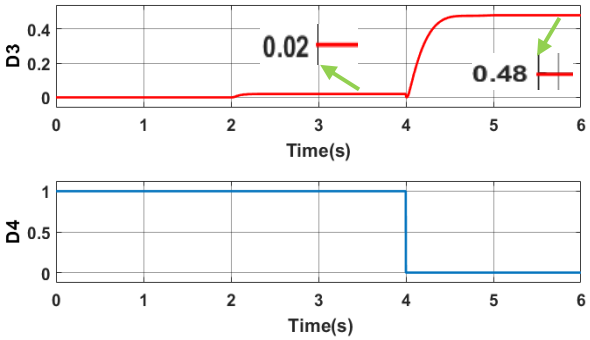

Figure 11. Duty cycles of S3 and S4

Based on Figure 12, it is confirmed that FC works at maximum power due to I_{L1}=225A in the first mode, I_{L1}=133A in the second mode, and I_{L1}=86A in the third mode. Since I_{L1} is the exact I_{FC}, as expected, the FC operates at maximum power. The current of first (I_{L1}) and second (I_{L2}) sources, output voltage of DC-DC converter (V_O), and the current of the battery ($I_{battery}$) have been shown in Figure 12. Proper transient-

state, suitable overshoot and undershoot of DC-DC converter state-variables, and reference tracking can be clearly seen in Figure 12, which is the result of the appropriate operation of the control system.

Figure 13 depicts the output voltage of the inverter. Figure 14 verifies that PV operates at maximum power. To prove that the inverter managed to produce a +90° phase difference in each mode, the output voltage of the inverter must be examined by FFT analysis. In all the modes, the voltage amplitude of the grid is assumed to be 100 V with a 60Hz frequency. Since all the calculations are based on amplitude, a 3/2 factor appears in basic equations.

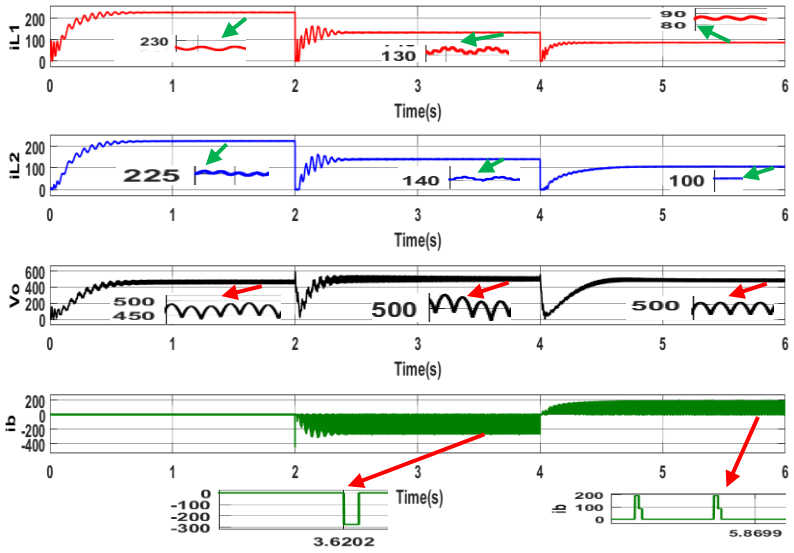

Figure 12. Output of the hybrid DC-DC converter

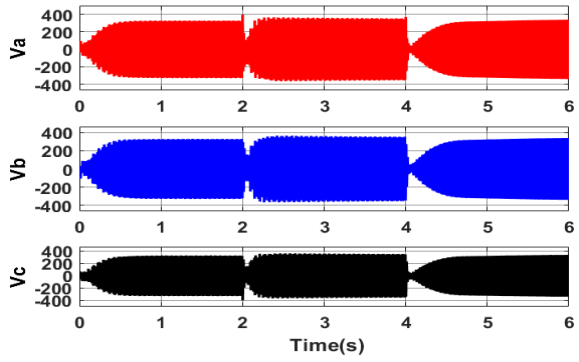

Figure 13. Output voltage of the inverter

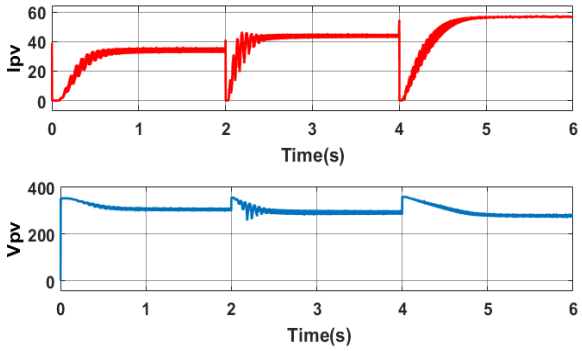

Figure 14. Output voltage and current of the PV

First-mode simulation $0 \le t \le 2$; Figure 15 represents the output voltage of the inverter. As expected, the fundamental harmonic has a +90° phase difference, and it causes the maximum power of PV and FC to be transferred to the AC side or gird side. A simple phase shift can produce the desired phase difference in the inverter. Figure 16 shows the FFT analysis of the current of the inverter (I_{an}).

FFT analysis in Figure 15 (a) and Figure 15 (b) confirms that the inverter produces a +90° phase difference, according to:

$$P_{12(3\varphi)} = \frac{3}{2}\frac{V_1 V_2}{X_L}\sin\delta \xrightarrow{V1=300.3V2=100XL=2.64\Omega} P_{12(3\varphi)} = 17069W$$

On the other hand, FFT analysis gives the phase differences between current and voltage:

$$S_{in\,v(3\varphi)} = \frac{3}{2} VI^* \xrightarrow{V=300.3\angle+90^o I=120\angle 18.4^o}$$
$$S_{in\,v(3\varphi)} = \frac{3}{2} \times (300.3) \times (120)\angle 90^o - (180 + 18.4)^o$$
$$S_{in\,v(3\varphi)} = -17063 - j51290.5$$

P_{12} confirms S_{inv}, which means that the inverter transfers 17063 W of active power to the grid. Only a 6W difference between S_{inv} and P_{12} is originated from numerical errors, which is acceptable in this range of power.

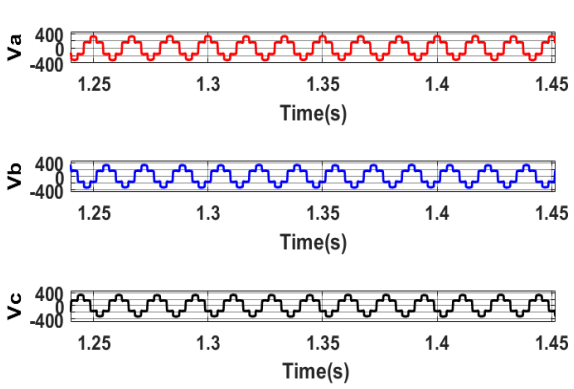

(a)

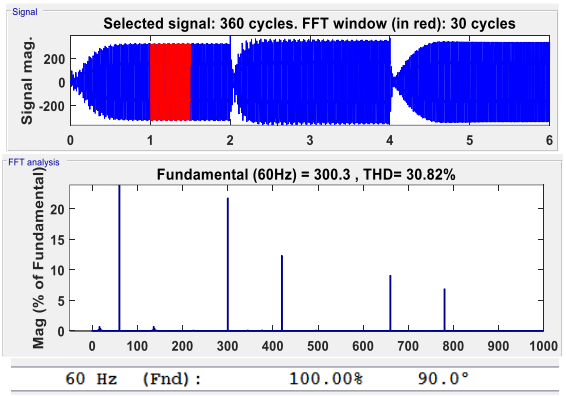

(b)

Figure 15. FFT analysis of V_{an} in the first mode, (a) inverter output voltage; (b) fundamental component amplitude

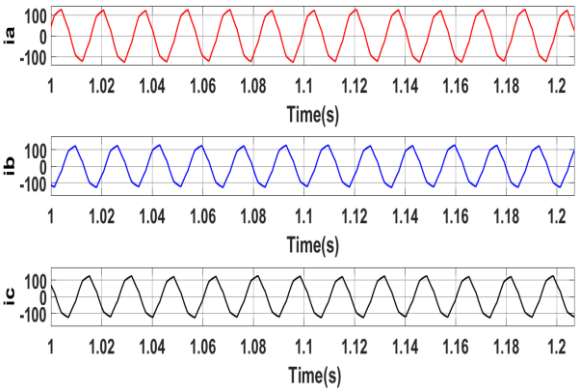

(a)

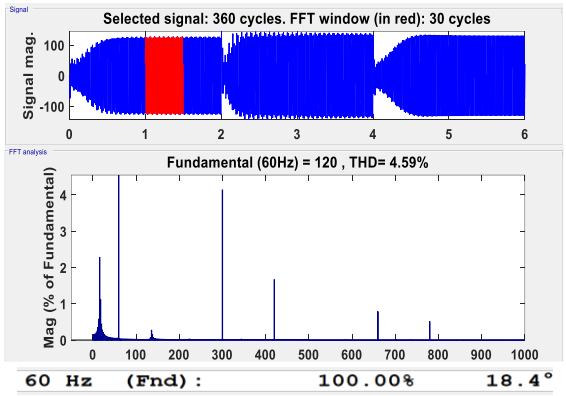

(b)

Figure 16. FFT analysis of I_{an} in the first mode, (a) inverter output current; (b) fundamental component amplitude

Second-mode simulation $2 \leq t \leq 4$; Figure 17 (a) and Figure 17 (b) presents an FFT analysis of V_{an}. It verifies that the inverter produces a +90° phase difference. Similar to the first mode, Figure 18 (a) and Figure 18 (b) shows the FFT analysis of the current of inverter (I_{an}).

$$P_{12(3\varphi)} = \frac{3}{2}\frac{V_1 V_2}{X_L} sin\,\delta \xrightarrow{V1=325.3\angle+90^O V2=100\angle 0^O XL=2.64} P_{12(3\varphi)} = 18490.4$$

S_{inv} can be calculated from the FFT analysis in the second mode according to Figure 17 and Figure 18:

$$S_{in\,v(3\varphi)} = \frac{3}{2} VI^* \xrightarrow{Van=325..3\angle+90^o ian=129.1\angle 17.1^o}$$
$$S_{in\,v(3\varphi)} = \frac{3}{2} \times 325.3 \times 129.1\angle - 107.1^o$$
$$S_{in\,v(3\varphi)} = -18523 - j60209.56$$

S_{inv} and P_{12} confirm each other well. A 32W difference is originated from numerical errors, which is acceptable in this range of power. In all the equations, $V_1=V_{an}$ (the inverter voltage) and $V_2=V_{gird}$.

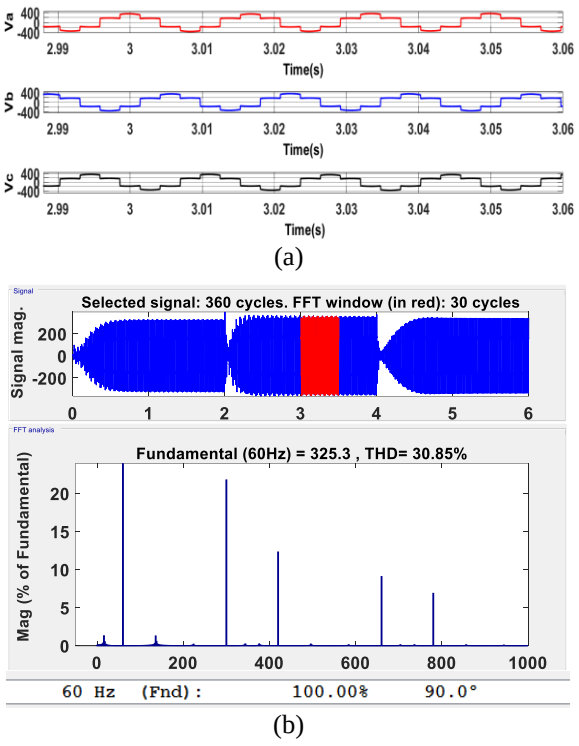

Figure 17. FFT analysis of V_{an} in the second mode, (a) inverter output voltage; (b) fundamental component amplitude

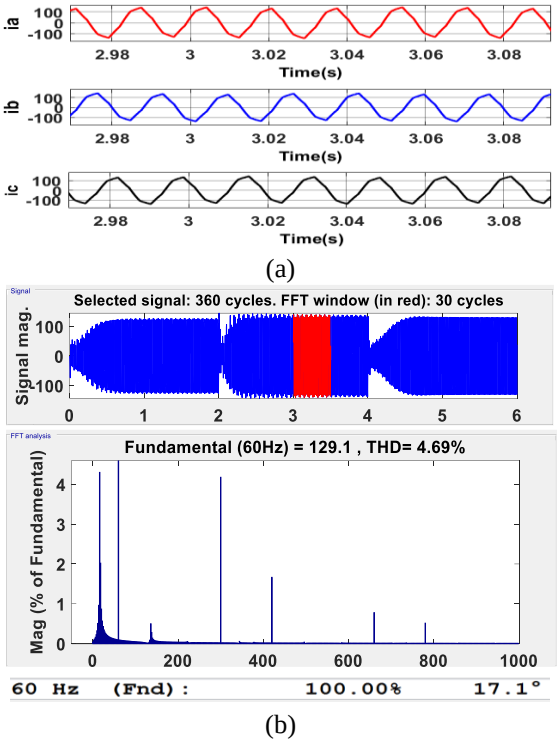

Figure 18. FFT analysis of I_{an} in the second mode, (a) inverter output current; (b) fundamental component amplitude

Third-mode simulation $4 \le t \le 6$; Figure 19 indicates the power of the battery in three modes. Similar to the first and second modes Figures 20 (a), (b) and Figures 21 (a), (b) depict the FFT analysis in the third mode. Figure 20 proves that the inverter creates a +90° phase difference.

$$P_{12(3\varphi)} = \frac{3}{2}\frac{V_1 V_2}{X_L}\sin\delta \xrightarrow[XL=2.64]{V1=314.3\angle+90^o \;\; V2=100^o} P_{12(3\varphi)} = 17865W$$

From FFT analysis

$$S_{inv(3\varphi)} = \frac{3}{2}VI^* \xrightarrow[X_L=2.64]{Van=314.3\angle+90^o \;\; ian=125\angle17.7^o}$$

$$S_{inv(3\varphi)} = \frac{3}{2}\times 314.3\times 125\angle -107.7^o$$

$$S_{inv(3\varphi)} = -17917.05 - j\,56141.53$$

S_{inv} and P_{12} match each other.

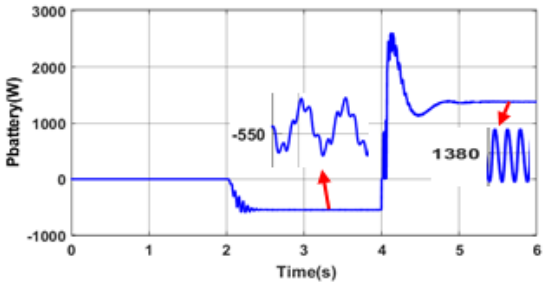

Figure 19. Power of the battery in all the modes

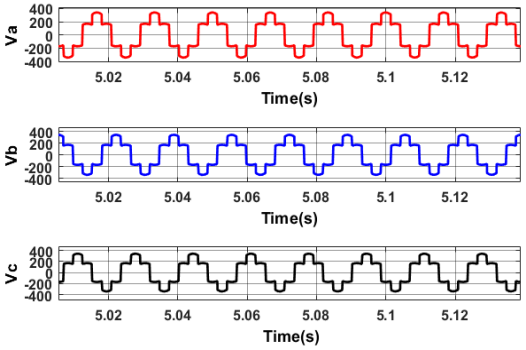

(a)

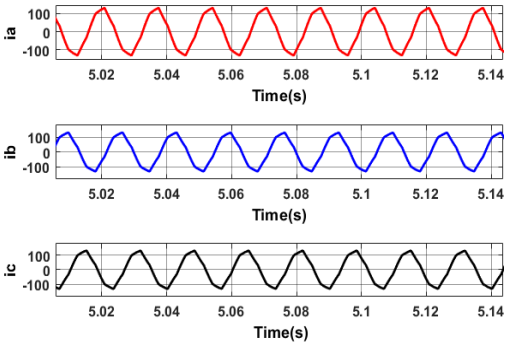

(a)

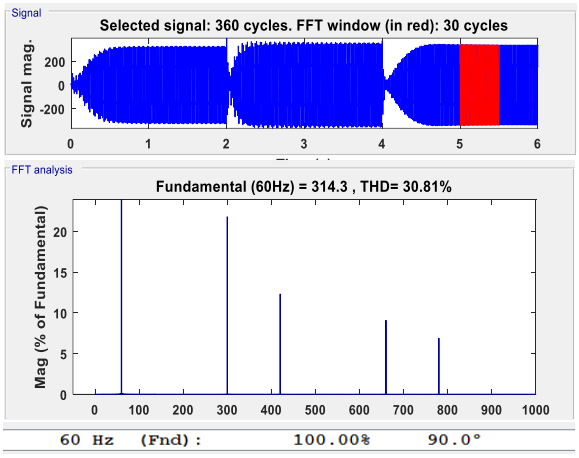

(b)

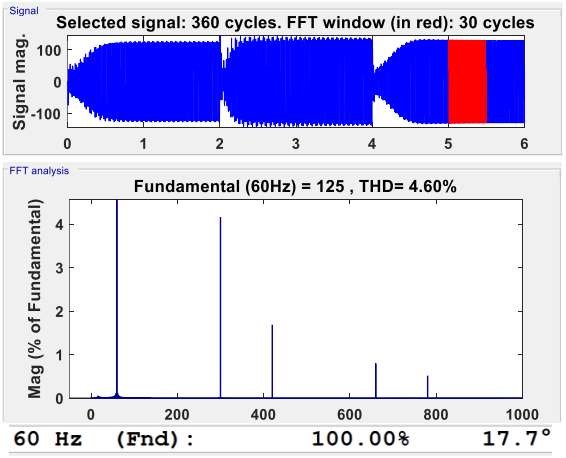

(b)

Figure 20. FFT analysis of V_{an} in the third mode, (a) inverter output voltage; (b) fundamental component amplitude

Figure 21. FFT analysis of I_{an} in the third mode, (a) inverter output current; (b) fundamental component amplitude

5. CONCLUSION

A new multivariable control technique was employed here to transfer the intended power to the grid side and extract the maximum power of PV simultaneously. The performance of the controller was examined under different scenarios. Simultaneous active power control and DC-link voltage regulation were possible for the proposed system.

In the proposed system, the three-phase inverter worked with a 50Hz switching frequency, due to which the leakage current of PV was no longer a problem. Power management and online operation can be performed more reliably in micro-grids and modern power systems with the proposed system. Still, more research on control and various power management strategies is required.

REFERENCES

[1] F. Nejabatkhah, S. Danyali, S. H. Hosseini, M. Sabahi, and S. M. Niapour, "Modeling and control of a new three-input DC–DC boost converter for hybrid PV/FC/battery power system," *IEEE Trans. Power Electron.*, vol. 27, no. 5, pp. 2309-2324, 2011, doi: 10.1109/TPEL.2011.2172465.

[2] X. Li, L. Guo, C. Hong, Y. Zhang, Y. W. Li, and C. Wang, "Hierarchical control of multiterminal DC grids for large-scale renewable energy integration," *IEEE Trans. Sustainable Enery*, vol. 9, no. 3, pp. 1448-1457, 2018, doi: 10.1109/TSTE.2018.2789465.

[3] R. R. Ahrabi, H. Ardi, M. Elmi, and A. Ajami, "A novel step-up multiinput DC–DC converter for hybrid electric vehicles application," *IEEE Trans. Power Electron.*, vol. 32, no. 5, pp. 3549-3561, 2016, doi: 10.1109/TPEL.2016.2585044.

[4] F. Akar, Y. Tavlasoglu, E. Ugur, B. Vural, and I. Aksoy, "A bidirectional nonisolated multi-input DC–DC converter for hybrid energy storage systems in electric vehicles," *IEEE Trans. Veh. Teclmol.*, vol. 65, no. 10, pp. 7944-7955, 2015, doi: 10.1109/TVT.2015.2500683.

[5] M. R. Banaei, H. Ardi, R. Alizadeh, and A. Farakhor, "Non-isolated multi-input–single-output DC/DC converter for photovoltaic power generation systems," *IET Power Electronics*, vol. 7, no. 11, pp. 2806-2816, 2014, doi: 10.1049/iet-pel.2013.0977.

[6] S. Danyali, S. H. Hosseini, and G. B. Gharehpetian, "New extendable single-stage multi-input DC–DC/AC boost converter," *IEEE Trans. Power Electron.*, vol. 29, no. 2, pp. 775-788, 2013, doi: 10.1109/TPEL.2013.2256468.

[7] B. Z. Ghavidel, E. Babaei, and S. H. Hosseini, "An improved three-input DC-DC boost converter for hybrid PV/FC/battery and bidirectional load as backup system for smart home," in *2019 10th International Power Electronics, Drive Systems and Technologies Conference (PEDSTC)*, 2019, doi: 10.1109/PEDSTC.2019.8697731.

[8] P. Mohseni, S. H. Hosseini, M. Sabahi, T. Jalilzadeh, and M. Maalandish, "A new high step-up multi-input multi-output DC–DC converter," *IEEE Trans. Ind. Electron.*, vol. 66, no. 7, pp. 5197-5208, 2018, doi: 10.1109/TIE.2018.2868281.

[9] N. Zhang, D. Sutanto, and K. M. Muttaqi, "A buck-boost converter based multi-input DC-DC/AC converter," in *2016 IEEE International Conference on Power System Technology (POWERCON)*, 2016, doi: 10.1109/POWERCON.2016.7753892.

[10] R. R. Ahrabi, Y. Wei Li, and F. Nejabatkhah "Hybrid AC/DC network with parallel LCC-VSC interlinking converters," *IEEE Trans. Power Syst.*, vol. 36, no. 1, pp. 722-731, 2020, doi: 10.1109/TPWRS.2020.3020235.

[11] J. Guo, I. Zenelis, X. Wang, and B.-T. Ooi, "WAMS-based model-free wide-area damping control by voltage source converters," *IEEE Trans. Power Syst.*, vol. 36, no. 2, pp. 1317-1327, 2021, doi: 10.1109/TPWRS.2020.3012917.

[12] X. Li *et al*., "A unified control for the DC–AC interlinking converters in hybrid AC/DC microgrids," *IEEE Trans. Smart Grid*, vol. 9, no. 6, pp. 6540-6553, 2017, doi: 10.1109/TSG.2017.2715371.

[13] X. Li, Z. Li, L. Guo, J. Zhu, Y. Wang, and C. Wang, "Enhanced dynamic stability control for low-inertia hybrid AC/DC microgrid with distributed energy storage systems," *IEEE Access*, vol. 7, pp. 91234-91242, 2019, doi: 10.1109/ACCESS.2019.2926814.

[14] D. Ranamuka, K. M. Muttaqi, and D. Sutanto, "Flexible AC power flow control in distribution systems by coordinated control of distributed solar-PV and battery energy storage units," *IEEE Trans. Sustainable Enery*, vol. 11, no. 4, pp. 2054-2062, 2019, doi: 10.1109/TSTE.2019.2935479.

[15] R. K. Varma, and M. Akbari, "Simultaneous fast frequency control and power oscillation damping by utilizing PV solar system as PV-STATCOM," *IEEE Trans. Sustainable Enery*, vol. 11, no. 1, pp. 415-425, 2019, doi: 10.1109/TSTE.2019.2892943.

[16] R. K. Varma, and H. Maleki, "PV solar system control as STATCOM (PV-STATCOM) for power oscillation damping," *IEEE Trans. Sustainable Enery*, vol. 10, no. 4, pp. 1793-1803, 2018, doi: 10.1109/TSTE.2018.2871074.

[17] F. Cadini, G. L. Agliardi, and E. Zio, "A modeling and simulation framework for the reliability/availability assessment of a power transmission grid subject to cascading failures under extreme weather conditions," *Applied Energy*, vol. 185, pp. 267-279, 2017, doi: 10.1016/j.apenergy.2016.10.086.

[18] F. Cadini, F. Cadini, and En Zio, "Estimation of rare event probabilities in power transmission networks subject to cascading failures," *Reliab. Eng. Syst. Saf.*, vol. 158, pp. 9-20, 2017, doi: 10.1016/j.ress.2016.09.009.

[19] P. Henneaux, "Probability of failure of overloaded lines in cascading failures," *International Journal of Electrical Power & Energy Systems*, vol. 73, pp. 141-148, 2015, doi: 10.1016/j.ijepes.2015.04.015.

[20] Y. Jia, Z. Xu, L. L. Lai, and K. P. Wong, "Risk-based power system security analysis considering cascading outages," *IEEE Trans Ind Informal.*, vol. 12, no. 2, pp. 872-882, 2015, doi: 10.1109/TII.2015.2499718.

[21] S. Mei, F. He, X. Zhang, S. Wu, and G. Wang, "An improved OPA model and blackout risk assessment," *IEEE Trans. Power Syst.*, vol. 24, no. 2, pp. 814-823, 2009, doi: 10.1109/TPWRS.2009.2016521.

[22] J. Qi, K. Sun, and S. Mei, "An interaction model for simulation and mitigation of cascading failures," *IEEE Trans. Power Syst.*, vol. 30, no. 2, pp. 804-819, 2014, doi: 10.1109/TPWRS.2014.2337284.

[23] P. Rezaei, P. Hines, and M. Eppstein, "Estimating cascading failure risk with random chemistry," *IEEE Trans. Power Syst.*, vol. 30, no. 5, pp. 2726-2735, 2014, doi: 10.1109/PESGM.2015.7285613.

[24] N. A. Salim, M. M. Othman, I. Musirin, M. S. Serwan, and S. Busan, "Risk assessment of dynamic system cascading collapse for determining the sensitive transmission lines and severity of total loading conditions," *Reliab. Eng. Syst. Saf.*, vol. 157, pp. 113-128, 2017, doi: Stendley Busan.

[25] A. Khaki-Sedigh and B. Moaveni, "Control configuration selection for multivariable plants," *Lecture Notes in Control and Information Sciences*, vol. 391, 2009, doi: 10.1007/978-3-642-03193-9.